Attenuation Correction of the X-Band Dual-Polarization Phased Array Radar Based on Observed Raindrop Size Distribution Characteristics

Jiabao Feng [1], Xiantong Liu [2], Feng Xia [2,*], Yu Zhang [1] and Xiaona Rao [2]

[1]   Guangzhou Meteorological Observatory, Guangzhou 511430, China; jbfeng@gd121.cn (J.F.); zhangyu@gd121.cn (Y.Z.)

[2]   Tornado Key Laboratory, Guangzhou Institute of Tropical and Marine Meteorology, China Meteorological Administration (CMA), Guangzhou 510641, China; xtliu@gd121.cn (X.L.); raoxn@gd121.cn (X.R.)

*   Correspondence: xiaf@gd121.cn

Abstract: X-band dual-polarization phased array radar (XPAR-D) possesses high resolution and plays a significant role in detecting meso- and micro-scale convective systems. However, the precipitation attenuation it endures necessitates an effective correction method. This study selected radar data from XPAR-D at the peak of Maofeng Mountain in Guangzhou during 16–17 May 2020 from three precipitation stages after quality control. Attenuation coefficients were calculated for different precipitation types through scattering simulations of raindrop size distribution (RSD) data. Next, an attenuation correction algorithm (MZ_H-K_{DP} method) was proposed for the radar reflectivity factor (Z_H) according to different raindrop types and compared to the Z_H-K_{DP} method currently in use. The results indicate that the attenuation amount of XPAR-D echoes depends on the attenuation path and echo intensity. When the attenuation path is shorter and the echo intensity is weaker, the amount of attenuation and correction is smaller. Difficulties arise when there are noticeable deviations, which are challenging to resolve using attenuation correction methods. Longer attenuation paths and stronger echoes highlight the advantages of the MZ_H-K_{DP} method, while the Z_H-K_{DP} method tends to overcorrect the bias. The MZ_H-K_{DP} method outperforms the Z_H-K_{DP} method for different precipitation types. The superior correction capability of the MZ_H-K_{DP} method provides a significant advantage in improving the performance of XPAR-D for the detection of extreme weather.

Keywords: X-band dual-polarization phased array radar; precipitation attenuation; precipitation types; raindrop size distributions

1. Introduction

Based on the wavelength, dual-polarization weather radars can be categorized into three types: S-band, C-band, and X-band. In recent years, X-band radar has found applications in severe weather observation due to its low cost, mobility, and high spatiotemporal resolution. However, electromagnetic waves with shorter wavelengths are more susceptible to attenuation. The scattering simulation results indicate that X-band electromagnetic waves have a one-way attenuation rate (A_H) more than 10 and 7–8 times higher than that of S-band and C-band electromagnetic waves, respectively [1]. Attenuation errors hinder the application of X-band radar in quantitative precipitation estimation and severe weather identification algorithms. Therefore, an effective method is needed to correct the attenuation.

Initially, Z_H attenuation correction was studied for the C-band radar. This included estimating the theoretical value of Z_H based on observed precipitation by relating the radar reflectivity factor to rain rate (Z-R relationships), followed by the calculation of A_H. However, uncertainties regarding the Z-R relationships limit the accuracy of this

method and render the correction results unstable [2]. To address this issue, Bringi et al. [3] discovered a linear correlation between A_H and the differential attenuation rate (A_{DP}) with specific differential phase (K_{DP}) from radar measurements, proposing its use for attenuation correction. K_{DP} is independent of factors such as radar calibration, rain zone attenuation, beam occlusion, and raindrop size distribution [4], effectively resolving the attenuation of dual-polarization radar with a shorter wavelength. Subsequently, a series of correction methods were developed, such as simple attenuation correction based on the differential phase (Φ_{DP}), the ZPHI correction, the Z_H-K_{DP} comprehensive method, the adaptive attenuation correction method for Φ_{DP}, and the hotspot correction method [3,5–9].

Despite its effectiveness, the K_{DP}-based (or Φ_{DP}-based) attenuation correction method has two limitations. Firstly, when the rainfall intensity is weak, the K_{DP} signal is often weak as well, leading to an error in the attenuation correction that is difficult to estimate. Hu et al. [7] compared the K_{DP} correction method with the Z_H method and concluded that while the K_{DP} correction method generally outperforms the Z_H method, correct errors of the K_{DP} method are larger when K_{DP} is small. To overcome this issue, a Z_H-K_{DP} combination method proved to be more effective by setting a K_{DP} threshold. Secondly, although K_{DP} has a linear relationship with A_H and A_{DP}, the attenuation coefficients are also influenced by raindrop size distribution, temperature, particle shape, strong echo regions, and Φ_{DP} measuring fluctuations [10–12]. Scattering simulations suggested that the attenuation coefficients of large raindrops are 2–3 times higher than those of smaller raindrops, and using a single coefficient can cause biases during attenuation correction [3]. Therefore, based on the quality control of Φ_{DP}, Wu [13] introduced RSD data to simulate the attenuation correction coefficients of raindrops with different types and applied K_{DP} to correct the C-band radar data (MK_{DP} method). The results revealed that MK_{DP} outperformed a single K_{DP} method.

Since 2017, supported by the Comprehensive Meteorological Observation and Experiment Project for Megacities of the China Meteorological Administration, observation experiments based on the X-band dual-polarization phased array radar (XPAR-D) have been conducted in Guangzhou. As of 2023, six radars have been erected and are currently in operation, playing a crucial role in monitoring rapidly occurring and dissipating meso- and micro-scale disastrous weather events, such as local heavy precipitation, tornadoes, microbursts, and hailstorms [14–16]. In addition, the China Meteorological Administration's Longmen Cloud Physics Field Experiment Base has deployed various cloud and precipitation observation instruments, including the 2D Video Disdrometer, to locations such as Fogang City, Guangzhou City, Enping City, and Yangjiang City in the Guangdong Province [17,18]. Through extensive experimentation, valuable observation data have been collected. In this study, the MZ_H-K_{DP} method, which is an improvement on the Z_H-K_{DP} method, is proposed based on a comprehensive analysis of the strengths and weaknesses of various correction methods and the locally available observational data. The MZ_H-K_{DP} method incorporates RSD data to simulate the attenuation coefficients for different raindrop types and is proposed to perform attenuation correction for the X-band radar. It will be compared with the Z_H-K_{DP} method currently in use.

This paper is structured as follows. Section 2 describes the materials and methods used in this study. The results are presented in Section 3, which includes the dual-polarization thresholds for different rain types, the attenuation coefficients for various precipitation types, and the confirmation of the corrected results. Finally, Sections 4 and 5 provide the discussion and primary conclusions of this study.

2. Materials and Methods

2.1. Raindrop Size Distribution (RSD)

The RSD data employed in this research were collected from the 2D Video Disdrometer installed in the Huangpu District of Guangzhou, which is managed by the Longmen Cloud Physics Field Experiment Base of the China Meteorological Administration. The measurement principle is based on the use of two perpendicular illuminants to scan and

determine the diameter of raindrops using a high-speed linear array. The sampling area is 10×10 cm^2, the measured particle size range is 0.1–8.1 mm (with 41 particle size segments at intervals of 0.2 mm), and the sampling time interval is $1/55,000$ s [19]. A comparative analysis of the RSD data using rainfall data from an automated weather station located at the side place in 2020 revealed a correlation coefficient of 96.7% between the two, and a bias of 4.5%. These results demonstrate the high accuracy of the RSD data.

2.2. X-Band Dual-Polarization Phased Array Radar (XPAR-D)

As of 2023, six XPAR-Ds are in operation in Guangzhou. They are situated at Maofeng Mountain, the Huadu District, the Panyu District, the Nansha District, the Conghua District, and the Zengcheng District, as shown in Figure 1. The XPAR-D located at Maofeng Mountain has been in operation for a relatively extended period, with stable data quality, and was erected at a higher height of 534 m to avoid interference from ground clutter, terrain obscuration, and other factors. Therefore, this study mainly uses data from the XPAR-D located at Maofeng Mountain to investigate the attenuation correction algorithm. The XPAR-D comprises 64 transmitter and receiver modules, with a transmission frequency of 9.4 GHz, a maximum detection distance of 42 km, and a resolution of 30 m. In the horizontal direction, scanning is performed mechanically, while in the vertical direction, a phased array scanning method is used. The scanning elevation range spans 0.9°–20.7° (with 11 elevation angles), and the scanning period is 90 s [7]. Table 1 provides an overview of the main performance indices of the radar.
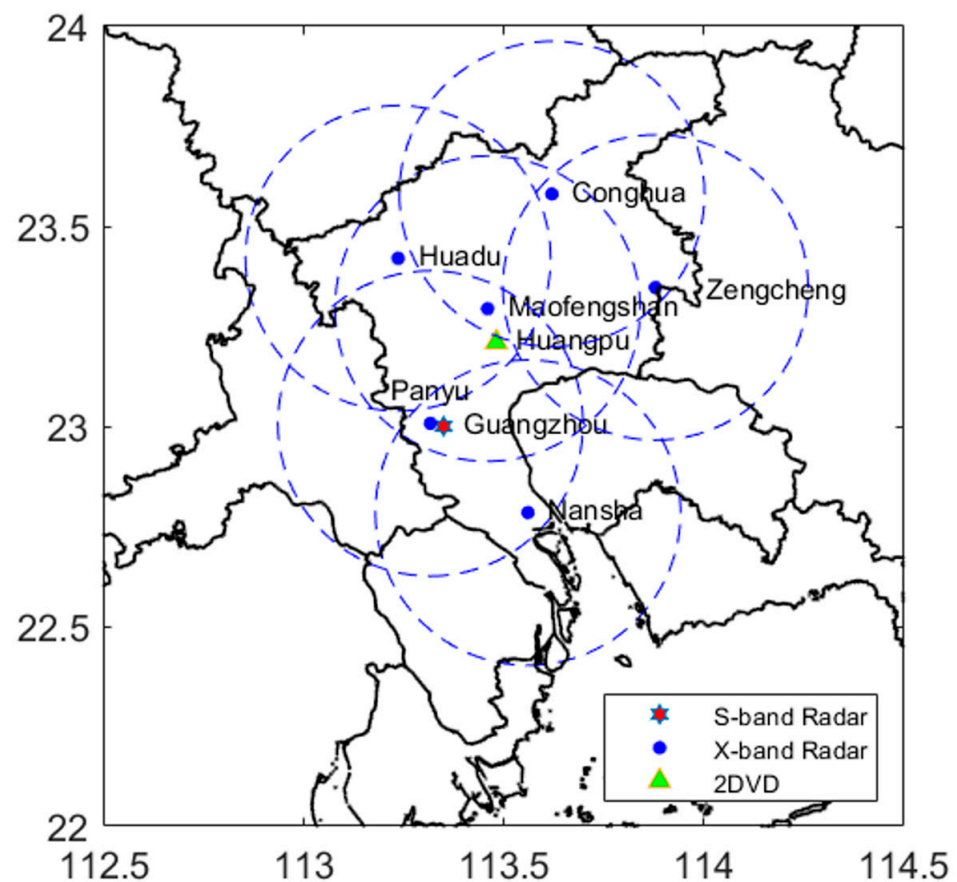

Figure 1. Spatial distribution of the 2D Video Disdrometer and radars.

Table 1. Main performance indices of the X-band dual-polarization phased array radar (XPAR-D).

Item	Parameter
Antenna type	One-dimensional array antenna
Peak power	256 W
Operating frequency	9.4 GHz
Polarization	Dual-pol/double-transmission and double receiving
Beam width (horizontal/vertical)	$3.6°/1.8°$
Volume-scanning period	90 s
Detection range	42 km
Resolution	30 m
Elevation range	$0.9°–20.7°$
Cut number	11
Peak power	256 W

2.3. S-Band Dual-Polarization Radar (SDPR)

Data from the Guangzhou S-band dual-polarization radar (SDPR), located in Panyu District, are used to validate the correction results in this study. The SDPR has been operational since May 2016, featuring double transmission and double reception in the horizontal and vertical directions. Its transmission frequency is 2.885 GHz. The maximum detection range is 230 km, and the resolution is 250 m. The volume scanning mode is the volume coverage pattern 21, the scanning elevation range spans from $0.5°$ to $9.9°$ (with 9 elevation angles), and the volume-scanning period is 6 min [20]. Both the SDPR and XPAR-D possess dual-polarization capabilities and can acquire horizontal/vertical reflectivity (i.e., Z_H/Z_V), radial velocity, velocity spectrum width, differential reflectivity factor (Z_{DR}), Φ_{DP}, K_{DP}, and correlation coefficient.

The current study utilizes the observation data matching method proposed by Wu [21] for different radar systems. This involves converting the polar coordinates of the XPAR-D data to geodetic coordinates, matching corresponding positions, and extracting parameters (Z_H, Z_{DR}, K_{DP}) of the Guangzhou SDPR radar system. Finally, the SDPR data are processed to fit the grid points of the XPAR-D and virtual observation data at equivalent locations are generated. Vertical linear interpolation of data from the two nearest SDPR elevation angles is applied to acquire corresponding data of the elevations of XPAR-D, considering that the SDPR's elevation distribution is uneven in the vertical direction and the XPAR-D's vertical sampling volume is greater.

2.4. Preprocessing of the X-Band Dual-Polarization Phased Array Radar Data

K_{DP}, a crucial parameter for the attenuation correction algorithm, can be derived from Φ_{DP}. However, radar noise and strong echo areas tend to affect the Φ_{DP} signal of the XPAR-D, necessitating data preprocessing before making use of K_{DP} data. Referring to the techniques proposed by Wu [13] and Chen [22], the primary steps of data preprocessing are presented in Figure 2. As a result of the preprocessing, the Φ_{DP} series becomes smoother and more continuous.

Figure 2. Flow chart for the quality control of the differential phase (Φ_{DP}) and obtaining the specific differential phase (K_{DP}).

Moreover, to reduce the influence of Φ_{DP} fluctuations on K_{DP}, the least-square method is used to calculate K_{DP}, as shown in Equation (1).

$$K_{DP} = \frac{\sum_{i=1}^{N} \left[\Phi_{DP}(r_i) - \overline{\Phi_{DP}} \right] (r_i - r_0)}{2 \sum_{i=1}^{N} (r_i - r_0)^2} \tag{1}$$

To obtain K_{DP} values for different reflectivity levels, the data series of Φ_{DP} in varying sizes $(r_i - r_0)$ is selected. When echoes register at less than 20 dBZ, a total of 45 bins are utilized. For echoes between 20 and 35 dBZ, 25 bins are used, and 15 bins are used for echoes greater than 35 dBZ. This method is more sensitive to heavy precipitation than the approach based on a fixed data series length.

2.5. Attenuation Correction Method

2.5.1. Z_H-K_{DP} Method

As the electromagnetic waves of the XPAR-D pass through rainy areas, their attenuation is relatively severe, requiring attenuation correction. K_{DP} can correct the horizontal reflectivity (i.e., Z_H). In particular, light rain conditions usually result in smaller K_{DP} values, leading to larger errors and an unknown effect on attenuation correction. To address this issue, the Z_H-K_{DP} correction method is presently utilized for correction, where the correction relationship is illustrated in Equation (2).

$$A_H = \begin{cases} a_1 K_{DP}, \sigma_1 \leq K_{DP} \leq \sigma_2 \\ \alpha Z_H^{\beta}, K_{DP} < \sigma_1 \text{ or } K_{DP} > \sigma_1 \end{cases} \quad (2)$$

When $K_{DP} < \sigma_1$ or $K_{DP} > \sigma_2$, the correction is conducted using the Z_H method, and coefficients α and β are taken as fixed values. When $\sigma_1 \leq K_{DP} \leq \sigma_2$, the K_{DP} method is used for correction, and the adaptive constraint correction method is used to fit a_1.

2.5.2. MZ_H-K_{DP} Method

Previous studies have shown that the attenuation coefficients of larger raindrops are 2–3 times higher than those of smaller ones [3], indicating that A_H values vary significantly depending on raindrop size. Therefore, attenuated correction based on different raindrop types is needed to obtain more precise results. In this study, data samples of different raindrop types are distinguished using RSD data. Threshold values of Z_H and K_{DP}, as well as attenuation coefficients for different raindrop types, are calculated using T-matrix, which is one of the most powerful and widely used methods for accurately computing scattering features of nonspherical particles [23–25]. Subsequently, attenuation amplitude (A_H) and corrected Z_H values are determined. The correction process of the MZ_H-K_{DP} method is demonstrated in Figure 3.

The Z_H, K_{DP}, and A_H calculated by T-matrix of RSD data are recorded as $Z_H{}'$ (dBZ), $K_{DP}{}'$ ($° \text{ km}^{-1}$), and $A_H{}'$ (dB km^{-1}), respectively, as shown in Equations (3)–(5) [26–28].

$$Z_{H,V}{}' = \frac{10^6 \lambda^4}{\pi^5 |k|^2} \int_0^{D_{max}} \sigma_{H,V} N(D) dD \quad (3)$$

$$K_{DP}{}' = 10^{-3} \frac{180}{\pi} \lambda \text{Re} \int_0^{D_{max}} [f_H(D) - f_V(D)] N(D) dD \quad (4)$$

$$A_{H,V}{}' = 4.343 \times 10^{-3} \int_0^{D_{max}} \sigma_{eH,V}(D) N(D) dD \quad (5)$$

where $Z_{H,V}$* denotes the horizontal and vertical reflectivity, λ (mm) the wavelength, $|K|^2 = \left| (m^2 - 1) / (m^2 + 2) \right|$ the dielectric constant of water, and $\sigma_{H,V}$ the horizontal and vertical backscattering cross-sections of raindrops. f_H and f_V represent the horizontal and vertical forward-scattering real parts, respectively. σ_{eH} and σ_{eV} indicate the horizontal and vertical extinction cross-sections, respectively.

```
┌──────────────────────────────┐
│ raindrop size distribution   │
│ data                         │
└──────────────────────────────┘
              │
              ▼
┌──────────────────────────────┐
│ classify different raindrop  │
│ types according to D0、NW、μ  │
└──────────────────────────────┘
              │
              ▼
┌──────────────────────────────┐
│ calculate ZH'、KDP'、AH' by   │
│ scattering simulation        │
└──────────────────────────────┘
        │                 │
        ▼                 ▼
┌────────────────┐  ┌────────────────┐
│ if small       │  │ if moderate    │
│ raindrop type  │  │ or large       │
│                │  │ raindrop type  │
└────────────────┘  └────────────────┘
        │                 │
        ▼                 ▼
┌────────────────┐  ┌────────────────┐
│ calculate      │  │ calculate      │
│ attenuation    │  │ attenuation    │
│ coefficient    │  │ coefficient    │
│ α、β according  │  │ a according    │
│ to AH'=α×ZH'^β │  │ to AH'=a×KDP'  │
└────────────────┘  └────────────────┘
        │                 │
        ▼                 ▼
┌────────────────┐
│ estimate the   │
│ raindrop type  │
│ of each bin of │
│ XPAR-D         │
└────────────────┘
        │                 │
        ▼                 ▼
┌────────────────┐  ┌────────────────┐
│ if small       │  │ if moderate    │
│ raindrop type  │  │ raindrop       │
│                │  │ or large       │
│                │  │ raindrop type  │
└────────────────┘  └────────────────┘
        │                 │
        ▼                 ▼
┌────────────────┐  ┌────────────────┐
│ calculate AH   │  │ calculate AH   │
│ according to   │  │ according to   │
│ AH=α×ZH^β      │  │ AH=a×KDP       │
└────────────────┘  └────────────────┘
        │                 │
        ▼                 ▼
┌──────────────────────────────┐
│ obtain ZH (cor) after        │
│ correction                   │
└──────────────────────────────┘
```
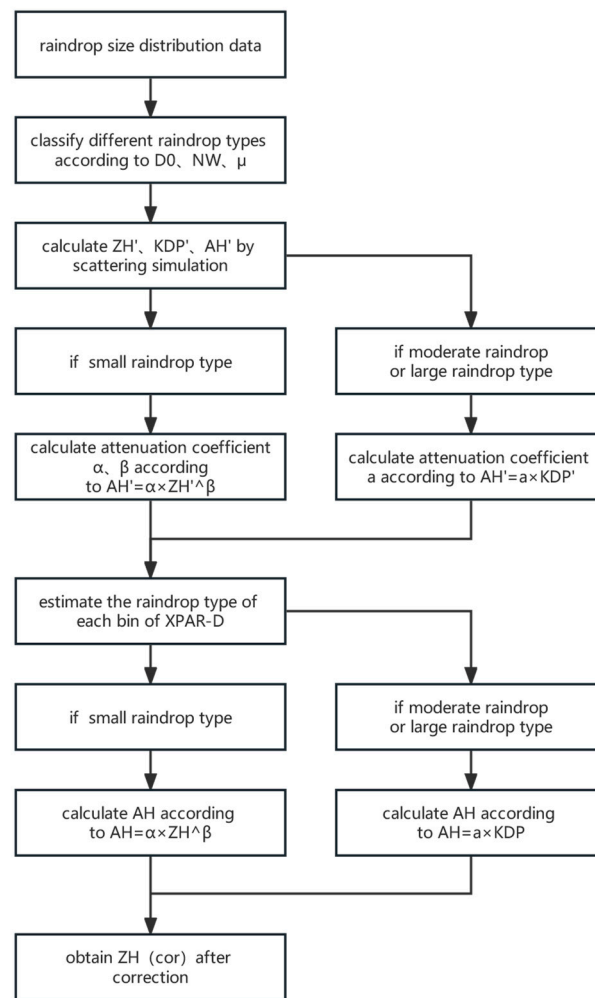
Figure 3. Flow chart for the attenuation correction algorithm of the MZ_H-K_{DP} method.

3. Results

3.1. Dual-Polarization Parameter Thresholds for Raindrop Classification

Wu [13] utilized the median volume diameter (D_0), the normalized intercept parameter (N_W), and the shape parameter (μ) to categorize various types of raindrops (Table 2). In this study, D_0, N_W, and μ are calculated, and each RSD sample is classified according to the threshold values listed in Table 2.

Table 2. RSD parameter thresholds for raindrop classification.

Raindrop Types	D_0 (mm)	N_W (mm^{-1} mm^{-3})	μ
Small Raindrop	$0.5 \leq D_0 \leq 1.4$	$10^3 \leq N_W \leq 21 \times 10^3$	$-1 \leq \mu \leq 5$
Moderate Raindrop	$1.2 \leq D_0 \leq 2.0$	$10^3 \leq N_W \leq 10^4$	$-1 \leq \mu \leq 5$
Large Raindrop	$1.7 \leq D_0 \leq 3.2$	$10^3 \leq N_W \leq 9 \times 10^3$	$-1 \leq \mu \leq 5$

Using scattering simulations, the Z_H' and K_{DP}' values for different raindrop types were calculated, and their frequency distributions are displayed in Figure 4. The results indicate a power function relationship between Z_H' and K_{DP}', and the high-value ranges of the Z_H'-K_{DP}' frequency differ notably among various raindrop types. The Z_H'-K_{DP}' values (Table 3), therefore, enable accurate differentiation between the raindrop types.
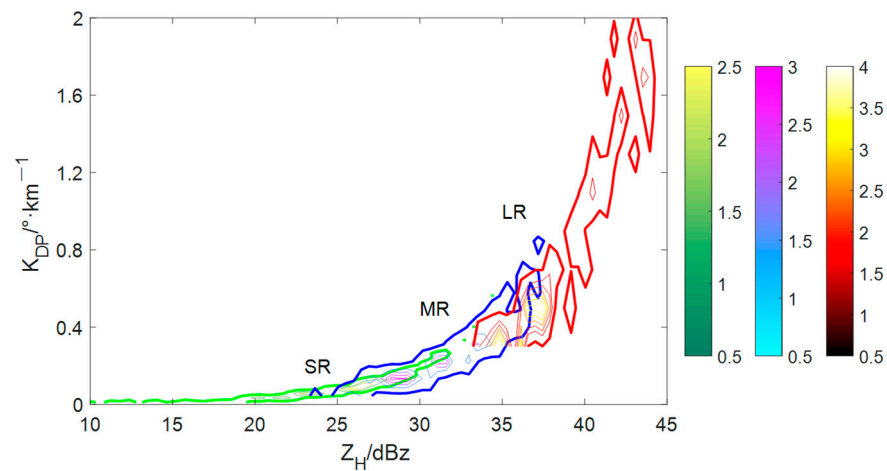
Figure 4. Frequency distributions of Z_H'-K_{DP}' from scattering simulations for different raindrop types, where SR represents a small raindrop type, MR represents a moderate raindrop type, and LR represents a large raindrop type.

Table 3. Dual-polarization parameter thresholds for raindrop classification.

Raindrop Types	Z_H	K_{DP}
Small Raindrop	$10 \leq Z_H < 30$	$0 \leq K_{DP} < 0.22$
Moderate Raindrop	$30 \leq Z_H < 36$	$0.22 \leq K_{DP} < 0.56$
Large Raindrop	$36 \leq Z_H < 60$	$0.56 \leq K_{DP} < 2$

In prior research, three dual-polarization parameters (Z_H, Z_{DR}, and K_{DP}) were typically employed together to differentiate between various raindrop types [22,29]. However, in this study, the correlation coefficient of Z_{DR} between the XPAR-D and the RSD simulations is only 0.2 at the same location, with an average error of -1.4 dB. This suggests poor data quality of the Z_{DR} observed by the XPAR-D. Accordingly, only two parameters, Z_H and K_{DP}, are utilized as thresholds in the present investigation.

3.2. Attenuation Coefficients of Different Raindrop Types

In this research, the attenuation coefficients of α, β, and a are calculated using A_H', Z_H', and K_{DP}' from the scattering simulations of raindrop size distribution. According to the MZ_H-K_{DP} method, the relationship can be expressed as Equation (6).

$$A_H' = \begin{cases} \alpha Z_H'^{\beta}, R \in SR \\ aK_{DP}', R \in MR, LR \end{cases} \tag{6}$$

When raindrops in the XPAR-D bins belong to the small raindrop type, correction is performed using the Z_H method. However, the K_{DP} method is utilized for correction for moderate or larger raindrop types. Figure 5 displays the attenuation coefficients of the various raindrops obtained from RSD scattering simulations. When the raindrop type is not classified, the correlation is 0.9 for K_{DP} (Figure 5d). For cases with various raindrop types, the correlation of A_H for Z_H and K_{DP} increases to 0.92 (Figure 5a) and 0.97 (Figure 5b,c), respectively, underscoring the necessity of conducting corrections based on different raindrop types. In addition, when raindrop-type identification is unfeasible, the K_{DP} method is utilized for correction and the attenuation coefficients are determined using K_{DP} and A_H from all samples (Figure 5d).
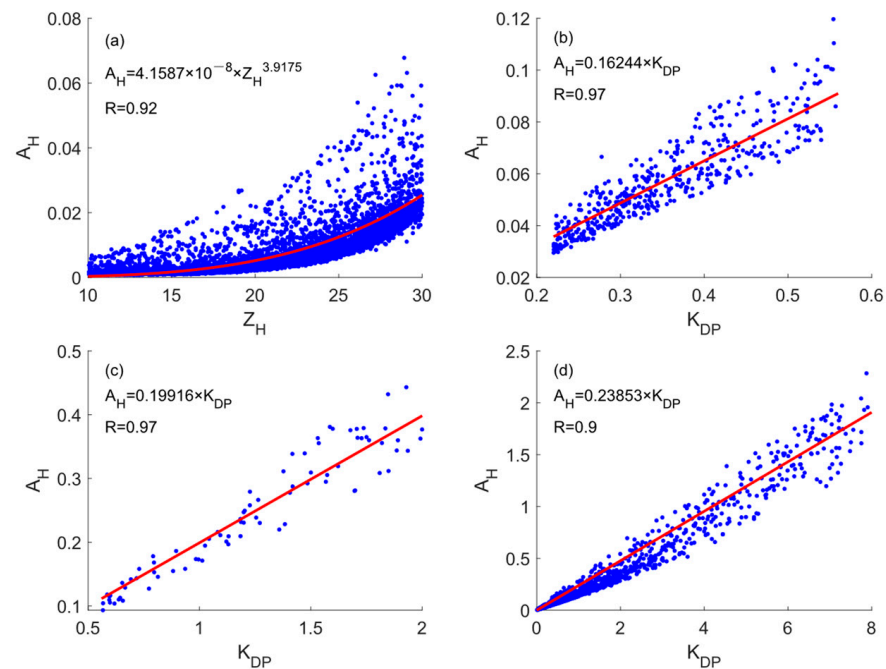
Figure 5. Attenuation coefficients and their fitting for (**a**) small raindrop type, (**b**) moderate raindrop type, (**c**) large raindrop type, and (**d**) all raindrop types.

Using the Z_H and K_{DP} values of the XPAR-D and their respective attenuation coefficients, the attenuation correction of Z_H is accomplished by computing the A_H of each bin. The correction relationship is indicated in Equation (7).

$$10\lg[Z_{H-\text{cor}}(r)] = 10\lg[Z_H(r)] + 2\int_0^r A_H(r)\text{ds} \tag{7}$$

where Z_H and Z_{H_cor} denote the reflectivity factors before and after correction, respectively, s represents the distance of the radar, and r indicates the distance variable (unit: km).

3.3. Verification of Correction Results

This study selects the precipitation process occurring from 16 to 17 May 2020, for a case study. Affected by an upper-level trough and shear line, Guangdong experienced widespread intense convective weather during this period. The convective activity commenced in northern Guangdong from 08:00 (UTC+8) on 16 May to 02:00 (UTC+8) on 17 May. Subsequently, convection in western Guangdong began to spread from the northwest to the southeast, while convection in eastern Guangdong gradually shifted from the southwest to the northeast. From 02:00 (UTC+8) to 10:00 (UTC+8) on 17 May, a convective pause period followed the previous energy release. From 10:00 (UTC+8) on 17 May to 04:00 (UTC+8) on 18 May, widespread strong convection moved from west to east, resulting in short-term heavy precipitation over a vast area. This was accompanied by gale-force winds.

The Guangzhou radar data underwent three rounds of analysis, at 19:06 (UTC+8) on 16 May 2020, 21:12 (UTC+8) on 17 May 2020, and 21:54 (UTC+8) on 17 May 2020. Figure 6 showcases the reflectivity factor during these times. Interestingly, when heavy precipitation occurs locally (Figure 6a), the convective cells exhibit a high intensity, reaching 50–55 dBZ at their peak. However, these cells are isolated and have a smaller area. As the precipitation transitions into the stratocumulus mixed stage (Figure 5b,c), the convective system organizes itself, and the strength of the cells is maintained. Furthermore, the northeastward movement of convective cells becomes swifter. Consequently, the frontal heavy echo region diminishes, leaving a vast expanse of stratiform precipitation at the rear.
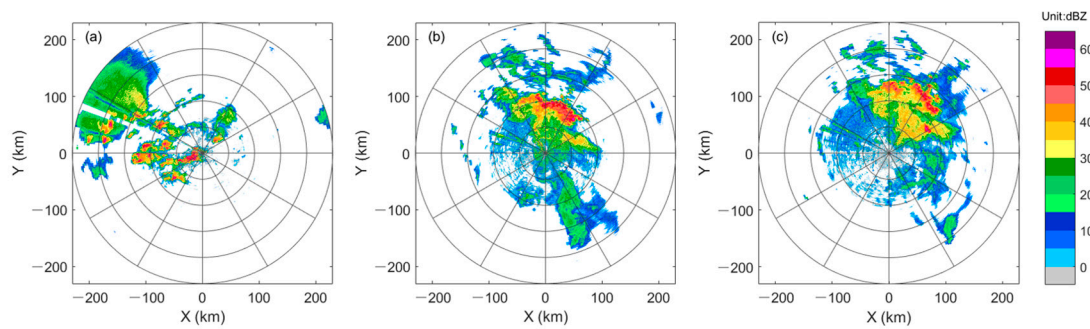
Figure 6. The radar reflectivity factor (Z_H) at the 1.5° elevation of the S-band dual-polarization radar (SDPR) at (**a**) 19:06 (UTC+8) on 16 May, (**b**) 21:12 (UTC+8) on 17 May, and (**c**) 21:54 (UTC+8) on 17 May 2020.

The Z_H comparisons between SDPR and XPAR-D at three typical times (Figure 7) reveal a typical instance of locally intense rainfall occurring at 19:06 on 16 May (Figure 7a–d). The short attenuation path results in minor differences in Z_H between XPAR-D and SDPR (Figure 7a,b). However, attenuation mostly affects the strong echo area adjacent to the radar center (x in Figure 7b). XPAR-D fails to depict an area in which the strong echoes extend beyond 50 dBZ.
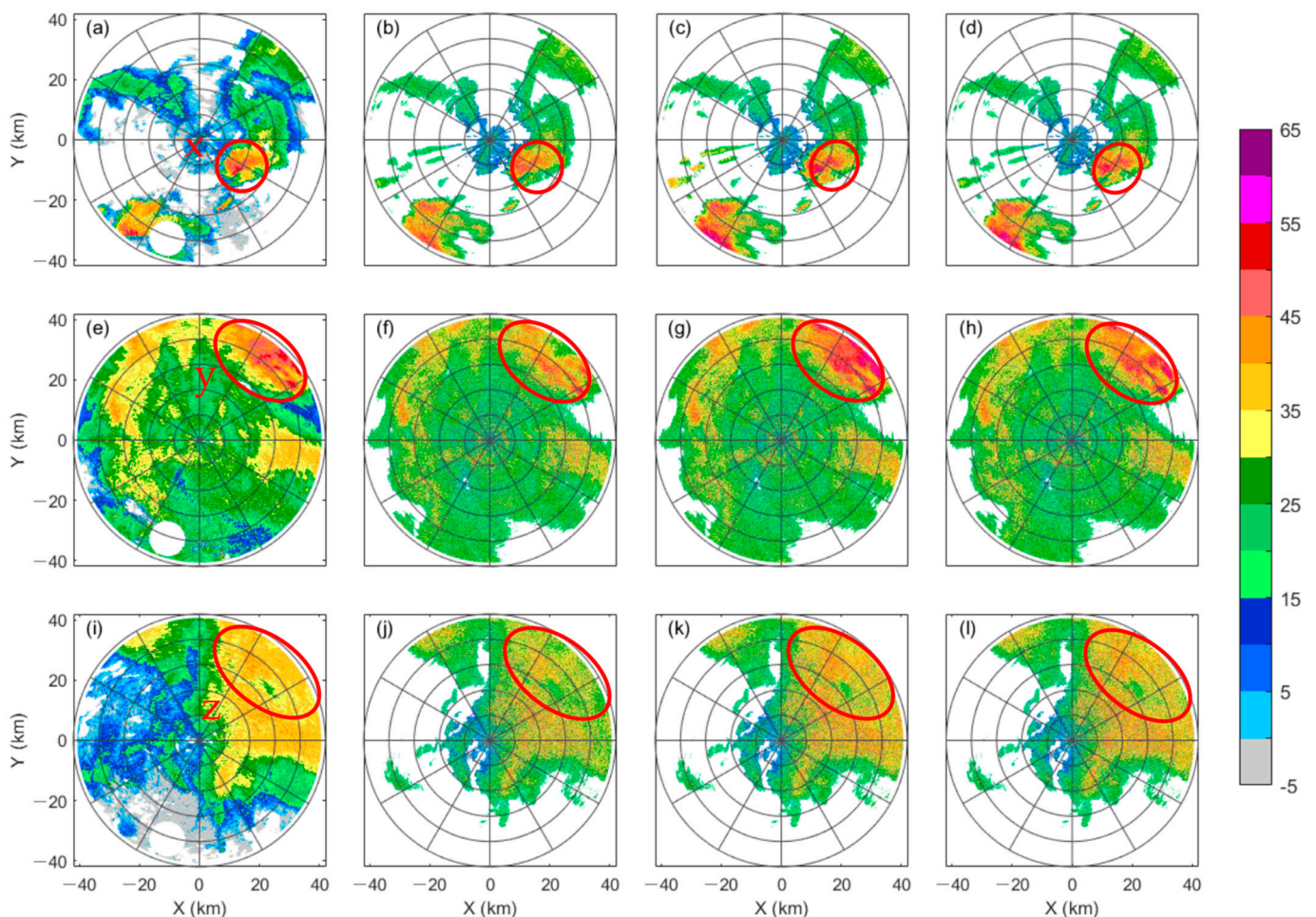
Figure 7. Comparison of the Z_H at the 2.7° elevation angle from (**a,e,i**) the SDPR data and from the XPAR-D data (**b,f,j**) before correction and after correction with (**c,g,k**) the Z_H-K_{DP} method and (**d,h,l**) the MZ_H-K_{DP} method at (**a–d**) 19:06 (UTC+8) on 16 May, (**c–h**) 21:12 (UTC+8) on 17 May, and (**i–l**) 21:54 (UTC+8) on 17 May 2020.

At 21:12 (Figure 7e–h) and 21:54 (Figure 7i–l) on 17 May, we can identify typical patterns of stratocumulus and stratiform precipitation. Due to the longer attenuation path and more extensive echo region, the XPAR-D detection of Z_H (Figure 7f–j) generally exhibits smaller values than the SDPR detection (Figure 7e–i), particularly for strong echoes that are distant from the radar centers. In situations involving stratocumulus precipitation, the distant, high-intensity echoes detected by the SDPR reach 45–55 dBZ (y in Figure 7e), while for the XPAR-D, they range from 25 to 50 dBZ (y in Figure 7f). This implies that they are 10–20 dBZ less than the SDPR. Additionally, the weaker the echoes in the same distance detected by the SDPR, the smaller the deviation between the two radars (z in Figure 7j).

The various attenuation correction algorithms exhibit different correction effects depending on the scenario. In the case of stratiform precipitation, both the Z_H-K_{DP} and MZ_H-K_{DP} methods yield good correction results for XPAR-D data (Figure 7k,l), with relatively minor differences.

For instances of local heavy rainfall, despite the intense echoes, the deviations between the XPAR-D and SDPR detections remain small due to the short attenuation path. The XPAR-D echoes near the radar center tend to be weaker (x in Figure 7b). After the MZ_H-K_{DP} correction, the strongest echo value of the XPAR-D is in good agreement with that of the SDPR, and the strong echo area expands slightly (x in Figure 7d). However, after the Z_H-K_{DP} correction, the strongest echo of the XPAR-D reaches 55–60 dBZ, which is an overcorrection, and the strong echo region increases (x in Figure 7c).

Regarding stratocumulus precipitation, the attenuation path of strong echoes is longer, with attenuation ranging from 5 to 10 dBZ and possibly up to 20 dBZ for the strong echoes that are distant from the radar center (y in Figure 7f). After the MZ_H-K_{DP} correction, the strong echo area aligns well with that of the SDPR (y in Figure 7h), while the Z_H-K_{DP} method overcorrects the echoes (y in Figure 7g). In conclusion, the MZ_H-K_{DP} method outperforms the Z_H-K_{DP} method.

The averaged Z_H values across various azimuths are utilized for quantitative comparisons (Figure 8). The results show that after correction, the Z_H curves of different precipitation scenarios almost match the original Z_H curve in the initial 1/2–2/3 segments of the attenuation path, revealing that the attenuation of the XPAR-D echoes is minimal during this time. Hence, it becomes difficult to diminish the deviations between the SDPR and the XPAR-D through attenuation correction. In the latter 1/2–1/3 segments of the attenuation path, the attenuation of the XPAR-D echoes increases with distance, and the differences between the corrected Z_H curve and the original Z_H curve gradually become more prominent.

Concerning stratiform precipitation (Figure 8a) and local heavy precipitation (Figure 8c), the disparities between the two correction methods are minor. Both methods exhibit commendable performance for the correction of stratiform precipitation, while the correction outcome is fair for local heavy precipitation. Concerning stratocumulus precipitation (Figure 8b), the deviations between the two correction methods intensify with distance. Significantly, the Z_H curve corrected by the MZ_H-K_{DP} method bears a closer resemblance to the SDPR Z_H curve, while the Z_H-K_{DP} method correction results show prominent discrepancies.

To conclude, the amplitude of attenuation is dependent on the path length and echo intensity. Longer paths and stronger echoes lead to potential overcorrection of the Z_H-K_{DP} method and accentuate the benefits of the MZ_H-K_{DP} method.

Furthermore, by inspecting the Z_H values of all the times of three precipitation types during 16–17 May 2020, we quantitatively analyze the attenuation characteristics of different precipitation types and the performance of the correction algorithms. The statistical indicators employed are the correlation coefficient (R), root mean square error (RMSE), normalized absolute error (NAE), and normalized relative error (NRE). Comparing the Z_H values between XPAR-D and SDPR (Figure 9a,d,g), we discover that when the Z_H exceeds 40 dBZ, the XPAR-D detection values are lower than those of the SDPR for all three precipitation types, indicating notable attenuation for echoes beyond 40 dBZ. Nonetheless,

for Z_H values below 40 dBZ, distinct precipitation types display different attenuation characteristics. Specifically, the XPAR-D detections are relatively inferior for the stratocumulus precipitation (Figure 9d), the difference between the two radars is insignificant for the stratiform precipitation (Figure 9g), and the XPAR-D detections are better for the local heavy precipitation (Figure 9a).
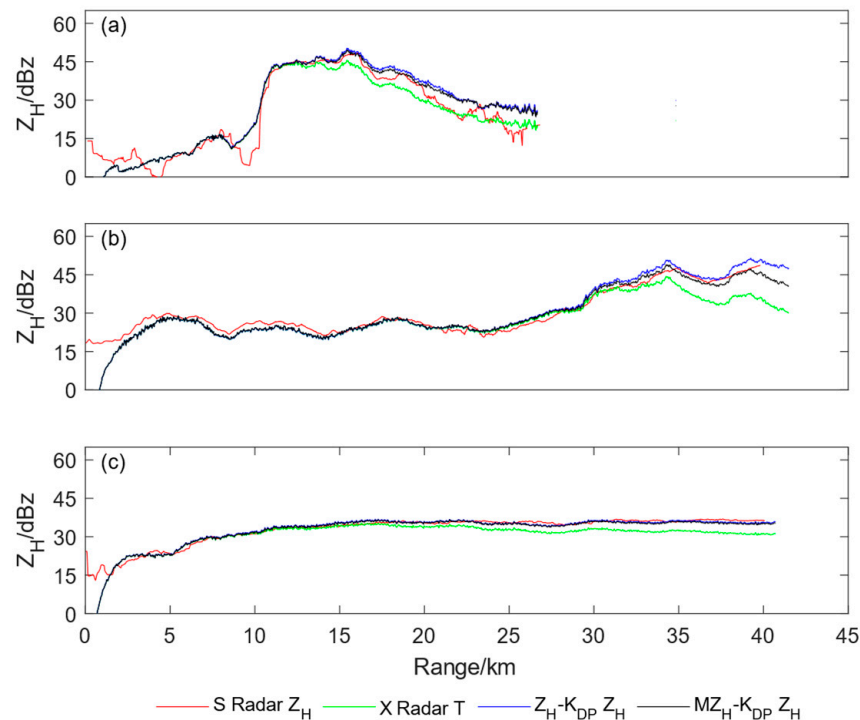

Figure 8. Comparisons of azimuth averaged Z_H at the 2.7° elevation angle in (**a**) the range of 110°–140° at 19:06 (UTC+8) on 16 May, (**b**) the range of 40°–65° average Z_H at 21:12 (UTC+8) on 17 May, and (**c**) the range of 80°–110° at 21:54 (UTC+8) on 17 May. The red line represents the Z_H from the SDPR, the green line indicates the original Z_H of the XPAR-D, and the blue and black lines denote the XPAR-D Z_H corrected by the Z_H-K_{DP} and MZ_H-K_{DP} methods, respectively.

The evaluation of the correction algorithm performance reveals that both MZ_H-K_{DP} and Z_H-K_{DP} methods provide only minor correction of echoes below 40 dBZ, and the former method performs somewhat better. For echoes exceeding 40 dBZ, the performance of the attenuation correction algorithms is strong, particularly for stratocumulus precipitation. Moreover, they exhibit some capability for attenuation correction of stratiform precipitation and local heavy precipitation.

In terms of locally heavy rainfall, we observe that the NRE values exceed zero, while positive deviations are present in XPAR-D echoes. Interestingly, these deviations are further amplified after attenuation correction. However, due to the efficient correction of strong echoes, we note significant improvement in R, RMSE, and NAE values post-correction. These outcomes indicate improved overall data quality upon correction, demonstrating that the MZ_H-K_{DP} method outperforms the Z_H-K_{DP} method.

For stratocumulus precipitation, the NRE values fall below zero, and XPAR-D echoes reflect distinct negative deviations. Notably, Z_H-K_{DP} method correction shows a decrease in negative deviations, though this is mainly attributable to the overcorrection of strong echoes and therefore does not imply that the Z_H-K_{DP} method correction is superior. Statistical indicators of R, RMSE, and NAE reveal that the MZ_H-K_{DP} method exhibits better performance.

Regarding stratiform precipitation, we note overall negative deviation as evidenced by NRE values falling below zero. We can reduce these values to nearly zero with effective

correction by both algorithms. However, various statistical indicators confirm that the MZ_H-K_{DP} method exhibits a better correction performance than the Z_H-K_{DP} method.
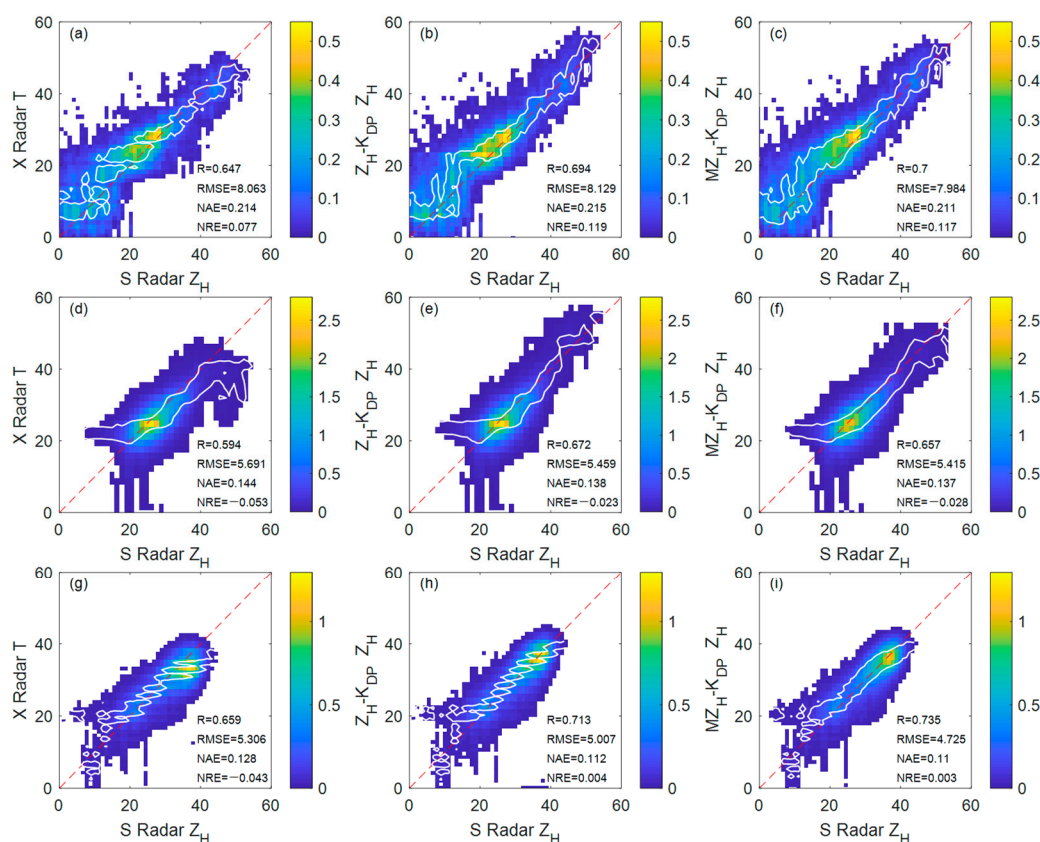

Figure 9. Comparisons of the Z_H probability density distribution of the SDPR data with the XPAR-D data (**a**,**d**,**g**) before and after the corrections of (**b**,**e**,**h**) the Z_H-K_{DP} method and (**c**,**f**,**i**) the MZ_H-K_{DP} method in terms of (**a**–**c**) local heavy precipitation, (**d**–**f**) stratocumulus precipitation, and (**g**–**i**) stratiform precipitation from 16 to 17 May 2020. Only colored areas with frequencies greater than 5% are displayed. "R", "RMSE", "NAE", and "NRE" denote the correlation coefficients, root mean square errors, normalized absolute errors, and normalized relative errors of the Z_H greater than 20 dBZ between the SDPR and the XPAR-D. The white line range shows the area with a maximum frequency standardization greater than 70%.

4. Discussion

The application of XPAR-D in China is still in its early stages, and there is relatively little research on attenuation correction algorithms compared to S-band, C-band, and X-band radars. Previous studies have shown that both the ZPHI and K_{DP} methods can achieve good correction effects, but considering the significant errors of K_{DP} in light rain, some studies will use both Z_H and K_{DP} for correction, which is slightly better than the K_{DP} method. This article proves that the MZ_H-K_{DP} method is better than the Z_H-K_{DP} method, so the MZ_H-K_{DP} method is effective among the attenuation correction algorithms above.

However, due to stability issues with the radar system, raindrop classification may be inaccurate, especially when the Z_H is small (<20 dBZ) and the signal-to-noise ratio is low. In addition, scattering simulation is based on 2D Video Disdrometer observations on the ground. In convective weather, the particles are complex in shape, motion state, and size, which can also cause instability in dual-polarization parameters. Various types of locally suitable precipitation coefficients should be sought using a large number of case statistics. Finally, due to the limited detection range and short operating time of XPAR-D, our comparison with the SDPR is restricted to a single precipitation event. As the quality of data from multiple radars gradually stabilizes in the future, the effectiveness of the

MZ_H-K_{DP} method needs to be tested further using multiple radars and multiple cases. All of the issues above must be addressed in future work.

5. Conclusions

In light of the significant attenuation observed in the XPAR-D during heavy precipitation, we selected data from Maofeng Mountain in Guangzhou for investigation across three typical precipitation types from 16 May to 17 May 2020. The data were collected at 19:06 (UTC+8) on 16 May, 21:12 (UTC+8) on 17 May, and 21:54 (UTC+8) on 17 May 2020. Utilizing Φ_{DP} data that had undergone stringent quality control, we studied the attenuation correction algorithm for Z_H and compared it with the algorithm presently employed in operations. The key findings from our study are as follows.

Before utilization, it is imperative to perform attenuation corrections on the XPAR-D data. Given that the attenuation coefficients of large raindrops are 2–3 times greater than their smaller counterparts, our study incorporates RSD data to derive dual-polarization thresholds for various raindrop types in Guangzhou. This approach yields corresponding attenuation coefficients and performs more accurate attenuation correction. Augmenting the process with raindrop-type classification renders improved fitting degrees of the attenuation coefficients, which increased from 0.77–0.90 to 0.92–0.97. This underscores the essentiality of raindrop-type classification for successful attenuation correction.

XPAR-D attenuation is dependent on the length of the propagation path and echo intensity. Longer attenuation paths and stronger echoes result in more pronounced attenuation, requiring greater amounts of attenuation correction. Differences between correction algorithms are mainly discernible in the latter half of the attenuation path. For moderate echo intensity (primarily stratiform precipitation), both the MZ_H-K_{DP} and Z_H-K_{DP} methods achieve commendable correction results. In cases of heightened echo intensity (primarily cumulus precipitation), the MZ_H-K_{DP} method substantially outperforms the Z_H-K_{DP} method, with results from the latter indicating significant overcorrection.

In contrast, attenuation is less evident when attenuation paths are shorter and echoes are weaker. Any noticeable deviations in the XPAR-D echoes at this time are not attributable to attenuation and therefore cannot be addressed using attenuation correction methods.

Author Contributions: Conceptualization, X.L. and J.F.; methodology, X.L. and J.F.; validation, X.L. and J.F.; formal analysis, J.F. and X.R.; investigation, J.F. and X.R.; resources, Y.Z.; data curation, Y.Z.; writing—original draft preparation, J.F.; writing—review and editing, F.X.; visualization, J.F.; supervision, F.X.; funding acquisition, X.L. and X.R. All authors have read and agreed to the published version of the manuscript.

Institutional Review Board Statement: Not applicable.

Informed Consent Statement: Not applicable.

Data Availability Statement: The data that support the findings of this study are available from the corresponding author upon reasonable request.

Conflicts of Interest: The authors declare no conflict of interest.

References

1. Park, S.G.; Bringi, V.N.; Chandrasekar, V.; Maki, M.; Iwanami, K. Correction of Radar Reflectivity and Differential Reflectivity for Rain Attenuation at X Band. Part I: Theoretical and Empirical Basis. *J. Atmos. Ocean. Technol.* **2005**, *22*, 1621–1632. [CrossRef]
2. Kampe, H.J.A.; Weickmann, H.K. Errors Inherent in the Radar Measurement of Rainfall at Attenuating Wavelengths. *J. Meteor.* **1954**, *11*, 58–67.

3. Bringi, V.N.; Keenan, T.D.; Chandrasekar, V. Correcting C-Band Radar Reflectivity and Differential Reflectivity Data for Rain Attenuation: A Self-Consistent Method With Constraints. *IEEE Trans. Geosci. Remote Sens.* **2001**, *39*, 1906–1915. [CrossRef]

4. Zrni, D.S.; Ryzhkov, A. Advantages of Rain Measurements Using Specific Differential Phase. *J. Atmos. Ocean. Technol.* **1996**, *13*, 454–464. [CrossRef]

5. Testud, J.; Bouar, E.L.; Obligis, E. Rain Profiling Algorithm Applied to Polarimetric Weather Radar. *J. Atmos. Ocean. Technol.* **1999**, *17*, 332–356. [CrossRef]

6. Bouar, E.L.; Testud, J.; Keenan, T.D. Validation of the Rain Profiling Algorithm "ZPHI" from the C-Band Polarimetric Weather Radar in Darwin. *J. Atmos. Ocean. Technol.* **2001**, *18*, 1819. [CrossRef]

7. Hu, Z.; Liu, L.; Chu, R.; Jin, R. Comparison of Different Attenuation Correction Methods and Theireffects on Estimated Rainfall Using X-band Dual Linear Polarimetric Radar. *Acta Meteorol. Sin.* **2008**, *66*, 251–261.

8. Gu, J.; Ryzhkov, A.; Zhang, P.; Neilley, P.; Knight, M.; Wolf, B.; Lee, D. Polarimetric Attenuation Correction in Heavy Rain at C Band. *J. Appl. Meteorol. Clim.* **2011**, *50*, 39–58. [CrossRef]

9. Xia, F.; Liu, X.; Zhang, T.; Feng, L.; Wan, Q.; Ou, G.; Zhang, X. Correction of Rainfall Attenuation and Partial Terrainblockage for C-band Dual Polarization Weather Radar. *J. Trop. Meteorol.* **2021**, *37*, 556–568. [CrossRef]

10. Bringi, V.N.; Chandrasekar, V.; Balakrishnan, N.; Zrnić, D.S. An Examination of Propagation Effects in Rainfall on Radar Measurements at Microwave Frequencies. *J. Atmos. Ocean. Technol.* **1990**, *7*, 829–840. [CrossRef]

11. Jameson, A.R. A Comparison of Microwave Techniques for Measuring Rainfall. *J. Appl. Meteorol. Clim.* **1991**, *30*, 32–54. [CrossRef]

12. Zrnic, D.S.; Keenan, T.D.; Carey, L.D. Sensitivity Analysis of Polarimetric Variables at a 5-cm Wavelength in Rain. *J. Appl. Meteorol. Clim.* **2000**, *39*, 1514–1526. [CrossRef]

13. Wu, L. Application Study of Mobile C-Band Dual-Polarization Radar Quality Control and QPE Using Raindrop Size Distribution. Ph.D. Thesis, Nanjing University of Information Science and Technology, Nanjing, China, 2014.

14. Zhang, Y.; Tian, C.; Fu, P.; Huang, H. Progress of Observation Experiment for X-band Dual-Polarization Phased Array Radars in Guangzhou. *Adv. MeteorSci. Technol.* **2020**, *10*, 80–85.

15. Zhang, Y.; Bai, L.; Meng, Z.; Chen, B.; Tian, C.; Fu, P. Rapid-Scan and Polarimetric Phased-Array Radar Observations of a Tornado in the Pearl River Estuary. *J. Trop. Meteorol.* **2021**, *27*, 6.

16. Zhang, Y.; Wu, S.; Li, H.; Hu, D.; Huang, H.; Fu, P.; Tian, C. Data Quality Analysis and Application of Guangzhou X-band Dual-Polarization Phased Array Radars. *J. Trop. Meteorol.* **2022**, *38*, 12.

17. Feng, L.; Xia, F.; Wan, Q.; Xiao, H.; Liu, X.; Zhang, T.; Li, H. Characteristics of the Raindrop Size Distribution in Two Squall Lines Measured by Two-Dimensional Video Disdrometer at Guangdong. *J. Trop. Meteorol.* **2019**, *35*, 812–821.

18. Liu, X.; Ruan, Z.; Hu, S.; Wan, Q.; Liu, L.; Luo, Y.; Hu, Z.; Li, H.; Xiao, H.; Lei, W.; et al. The Longmen Cloud Physics Field Experiment Base, China Meteorological Administration. *J. Trop. Meteorol.* **2023**, *29*, 1–15. [CrossRef]

19. Liu, X.; Li, H.; Hu, S.; Wan, Q.; Xiao, H.; Zheng, T.; Li, M.; Ye, L.; Guo, Z.; Wang, Y. A High-Precision and Fast Solution Method of Gamma Raindrop Size Distribution Based on 0-Moment and 3-Moment in South China. *J. Appl. Meteorol. Clim.* **2021**, *10*, 60. [CrossRef]

20. Chen, C.; Hu, Z.; Hu, S.; Zhang, Y. Preliminary Analysis of Data Quality of Guangzhou S-band Polarimetric Weather Radar. *J. Trop. Meteorol.* **2018**, *34*, 59–67.

21. Wu, C.; Liu, L.; Zhang, Z. Quantitative Comparison Algorithm between the S-band Phased Array Radar and the CINRAD/SA and Its Preliminary Application. *Acta Meteorol. Sin.* **2014**, *72*, 390–401.

22. Chen, W. Quantitative Precipitation Estimation by Dual Linear Polarization Radar Combined with Raindrop Spectrometer. Ph.D. Thesis, Chengdu University of Information Technology, Chengdu, China, 2020.

23. Feng, L.; Hu, S.; Liu, X.; Xiao, H.; Pan, X.; Xia, F.; Ou, G.; Zhang, C. Precipitation Microphysical Characteristics of Typhoon Mangkhut in Southern China Using 2D Video Disdrometers. *Atmosphere* **2020**, *11*, 975. [CrossRef]

24. Guo, Z.; Hu, S.; Liu, X.; Chen, X.; Zhang, H.; Qi, T.; Zeng, G. Improving S-Band Polarimetric Radar Monsoon Rainfall Estimation with Two-Dimensional Video Disdrometer Observations in South China. *Atmosphere* **2021**, *12*, 831. [CrossRef]

25. Lai, R.; Liu, X.; Hu, S.; Xiao, H.; Xia, F.; Feng, L.; Li, H. Raindrop Size Distribution Characteristic Differences During the Dry and Wet Seasons in South China. *Atmos. Res* **2022**, *266*, 105947. [CrossRef]

26. Aydin, K.; Zhao, Y.; Seliga, T.A. Rain-Induced Attenuation Effects on C-band Dual-Polarization Meteorological Radars. *IEEE Trans. Geosci. Remote Sens.* **1989**, *27*, 57–66. [CrossRef]

27. Tang, Q.; Xiao, H.; Guo, C.; Feng, L. Characteristics of the Raindrop Size Distributions and Their Retrieved Polarimetric Radar Parameters in Northern and Southern China. *Atmos. Res.* **2014**, *135/136*, 59–75. [CrossRef]

28. Ding, Y.; Wan, Q.; Yang, L.; Liu, X.; Xia, F.; Feng, L. Raindrop Size Distribution Parameters Retrieved from Xinfeng C-Band Polarimetric Radar Observations. *J. Trop. Meteorol.* **2020**, *26*, 275–285.

29. Huang, X.; Yin, J.; Ma, L.; Huang, Z. Comprehensive Statistical Analysis of Rain Drop Size Distribution Parameters and Their Application to Weather Radar Measurement in Nanjing. *Chinese J. Atmos. Sci.* **2019**, *43*, 691–704.